ACS APPLIED MATERIALS & INTERFACES

Research Article

www.acsami.org

Nanocolumnar Interfaces and Enhanced Magnetic Coercivity in Preferentially oriented Cobalt Ferrite Thin Films Grown Using Oblique-Angle Pulsed Laser Deposition

Devajyoti Mukherjee,* Mahesh Hordagoda, Robert Hyde, Nicholas Bingham, Hariharan Srikanth, Sarath Witanachchi, and Pritish Mukherjee

Center for Integrated Functional Materials (CIFM) & Department of Physics, University of South Florida, Tampa, Florida 33620, United States

Supporting Information

ABSTRACT: Highly textured cobalt ferrite (CFO) thin films were grown on Si (100) substrates using oblique-angle pulsed laser deposition (α-PLD). X-ray diffraction and in-depth strain analysis showed that the obliquely deposited CFO films had both enhanced orientation in the (111) crystal direction as well as tunable compressive strains as a function of the film thicknesses, in contrast to the almost strain-free polycrystalline CFO films grown using normal-incidence PLD under the same conditions. Using in situ optical plume diagnostics the growth parameters in the α-PLD process were optimized to achieve smoother film surfaces with roughness values as low as 1−2 nm as compared to the typical values of 10−12 nm in the normal-incidence PLD grown films. Cross-sectional high resolution transmission electron microscope images revealed nanocolumnar growth of single-crystals of CFO along the (111) crystallographic plane at the film−substrate interface. Magnetic measurements showed larger coercive fields (~10 times) with similar saturation magnetization in the α-PLD-grown CFO thin films as compared to those deposited using normal-incidence PLD. Such significantly enhanced magnetic coercivity observed in CFO thin films make them ideally suited for magnetic data storage applications. A growth mechanism based on the atomic shadowing effect and strain compression−relaxation mechanism was proposed for the obliquely grown CFO thin films.

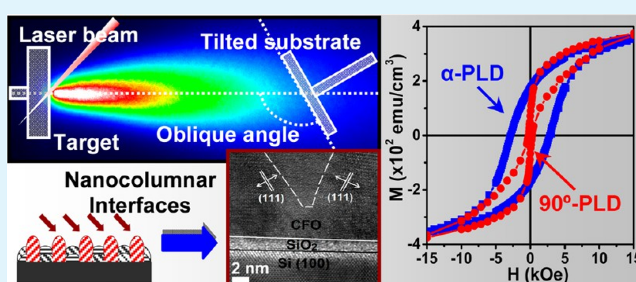

KEYWORDS: *glancing angle deposition, nanostructured thin films, strain, remnant magnetization, magneto-optic recording*

1. INTRODUCTION

Cobalt ferrite ($CoFe_2O_4$ or CFO) thin films have been studied extensively for their excellent magnetic properties such as high coercivity, moderate saturation magnetization (M_{sat}), large magnetic anisotropy and magentostriction as well as their remarkable chemical stability and mechanical hardness.[1,2] These factors make CFO thin films attractive candidates for a wide range of applications in high-density magnetic recording media,[3] magnetic tunnel junctions,[4] magnetostrictive sensors,[5] and magneto-optic devices.[6] The unique magnetic properties of CFO can be understood from its electronic and structural configurations. CFO has an inverse spinel crystal structure with a face-centered cubic unit cell, consisting of eight formula units where the Co^{2+} and Fe^{3+} ions are located on the octahedral and tetrahedral sites, respectively.[1] The eight Fe^{3+} ions in tetrahedral sites are aligned antiferromagnetically with respect to the remaining eight Fe^{3+} ions via superexchange interactions mediated by oxygen ions. Thus, the uncompensated Co^{2+} ions that have three unpaired electrons in their d-orbitals would give a theoretical M_{sat} value of 3 μ_B per Co^{2+} site for CFO.[2] However, in reality, it has been observed that extrinsic conditions such as residual strains in CFO thin films, can cause canting of the Fe^{3+} magnetic moments from their antiparallel configuration and consequently a change in the cation distribution in the crystal. This can result in the alteration of the effective magnetic moment in CFO systems and their coercivity. In this regard, some groups have reported on the tunable magnetic properties of CFO thin films by controlling their microstructure, grain size, film thickness, choice of substrate, and the lattice strains.[7−9] Several thin film deposition techniques such as molecular beam epitaxy (MBE),[9] pulsed laser deposition (PLD),[10] sputtering,[11] ion-beam deposition,[12] and sol−gel processing[13,14] have been used over the years to prepare CFO thin films. Among them the pulsed laser deposition (PLD) technique has been the most versatile in terms of CFO thin film growth because of its relatively low substrate temperature requirements[15] as compared to the high annealing temperatures in sol−gel processes[13,14] and the precise control of film crystallinity, whether polycrystalline[16] or epitaxial,[8] and thickness[7] that otherwise affect the magnetic

Received: May 10, 2013
Accepted: July 5, 2013
Published: July 5, 2013

ACS Publications © 2013 American Chemical Society

anisotropy[17,18] and residual strain[19] in CFO thin films. PLD also offers inherent simplicity in terms of in situ growth of multilayered thin films such as multiferroic heterostructures, where CFO layers are grown in combination with perovskite ferroelectric films.[20] As with all processes, one of the limiting factors of PLD has been the low coercivity observed in the as-deposited CFO thin films owing to their relatively larger grain sizes as compared to chemical techniques such as sol−gel processing.[21] Typically, PLD-grown CFO thin films require ex situ post annealing procedures to enhance their coercivity which is necessary for magnetic recording applications so that stray magnetic fields cannot easily flip the moments and destroy the stored information.[22] For industrial applications, it is desirable to grow CFO thin films with large coercivity on Si substrates to easily incorporate with existing technologies.

In this work, we have used an oblique-angle PLD technique to grow CFO thin films on Si substrates that exhibited superior surface qualities and enhanced magnetic properties as compared to films grown using normal-incidence PLD under the same conditions. High remnant magnetization and coercive fields observed in the obliquely grown CFO films make them ideally suitable for magnetic storage applications. These enhancements were attributed to the nanocolumnar interfaces and the compressive strains developed in the films as a result of oblique-angle deposition.

As opposed to a "normal" deposition where the angle between the vapor flux of the deposited material and the substrate is 90°, in "oblique" deposition the substrate is tilted so that the angle of deposition becomes greater than 90° (oblique) with respect to the target. Use of oblique-angle (or glancing) deposition in thermal evaporation processes has been reported earlier in the growth of "sculptured" thin films with three-dimensional microstructures.[23,24] It has also been used in sputtering processes for the growth of nanocolumnar single-component films of metals like W,[25] Cu,[26] and Co,[27] or semiconductors like Si,[28] where the nanocolumn formations were primarily attributed to the atomic shadowing effect.[29,30] However, because of the low adatom diffusion in the process, most of the obliquely deposited PLD films were amorphous and hence, there are very few reports on the oblique-angle PLD of crystalline multicomponent materials.[31] In fact, literature search shows only two reports on the oblique-angle PLD of multicomponent oxides. The first report was on the growth of nanostructured $YBa_2Cu_3O_x$ thin films using oblique-angle PLD by Wang et al.[32] More recently, Chen et al. have presented on the growth of tilted nanocolumnar films of the magnetic oxide $La_{0.7}Sr_{0.3}MnO_3$ by oblique-angle PLD.[33] These literature reports indicate that oblique-angle deposition of multi-component materials using PLD is complicated and requires precise control and optimization of the deposition parameters.

Here we have shown that using in situ optical diagnostics during film growth and through adjustments of the substrate tilt angles, deposition parameters and film thicknesses it is possible to control the crystal orientations, grain sizes, surface roughnesses, and residual strains in CFO thin films and thus achieve their enhanced and tunable magnetic properties. By comparing the results with CFO thin films grown under the same conditions using normal incidence PLD, we proposed a novel growth mechanism for the oblique-incident CFO thin films that could be extended to other material systems. Finally, the strain compression−relaxation mechanism that has been used to explain the tunable magnetic properties in CFO thin films provides new insight into the structure−property relationships of this technologically important hard magnetic material.

2. EXPERIMENTAL SECTION

CFO thin films were deposited on Si (100) substrates (with an ultrathin native amorphous SiO_2 layer on top) using oblique-angle pulsed laser deposition (α-PLD). A KrF excimer laser (Lambda Physik, λ = 248 nm) operating at 10 Hz was used to ablate a rotating compressed powder target of CFO prepared by standard pressing-sintering technique.[7,8] The laser beam was focused on the polished target surface with an angle of incidence of 45°, providing an energy density (or fluence) of 2−6 J/cm^2. The substrate was tilted so that the angle between the surface of the target and the surface normal of the substrate was 120° (oblique-angle) (as shown in Figure 1). Several

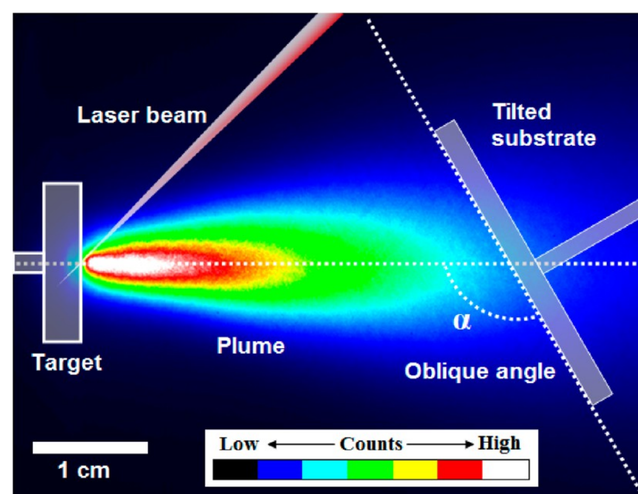

Figure 1. Time-integrated ICCD image of the total visible emission from the laser-induced plumes during the oblique-angle (α) PLD of CFO thin films. The position of the CFO target, the laser beam and the 120°-tilted substrate have been schematically drawn to-scale to show their real positions in space with respect to the plasma plume (see scale bar in figure).

steps were taken to minimize the thickness variations in the deposited films. First, the laser beam was focused onto a relatively large rectangular laser-spot-size of 2 mm × 3 mm on the target surface to enlarge the ablation volume;[34] second, the target-wobbling technique was employed with a wobble angle of 2−3°,[35] and finally, only small area substrates (1 cm × 1 cm) were used which were precisely placed such that the center of the ablated plumes aligned with the center of the substrates. Prior to depositions, the chamber was pumped to a base pressure of 1.0 × 10^{-6} Torr and the target was preablated for 2 min at 10 Hz to remove any surface contaminants. After the proper optimization of the growth parameters, finally, a series of CFO thin films of varying thicknesses from 50 to 400 nm were deposited at a substrate temperature of 450 °C in an ambient O_2 pressure of 10 mTorr using laser fluence of 2 J/cm^2. A distance of 4 cm was maintained between the substrates and the targets during deposition. After deposition, the films were cooled down to room temperature at 5 °C/min in an O_2 pressure of 10 mTorr. For comparison, CFO thin films were also deposited on Si substrates using normal-incidence PLD under the same conditions. Under the above conditions, the growth rates for obliquely incident CFO thin films were measured to be 0.5 Å/s whereas those for the normal-incidence films were found to be 1 Å/s.[7,8] To optimize the growth parameters in the α-PLD process, we observed the laser-ablated plasma plumes in situ and imaged them during the film growth process. For this purpose, an intensified charge-coupled detector (ICCD) imaging system (PI Acton PI-MAX:512 UNIGEN Digital ICCD Camera System, 512 × 512 pixels, <5 ns gating capability, spectral range 150−925 nm) set at 20 μs exposure

time was aligned normal to the plume propagation direction to capture the total visible emission from the laser-ablated plumes in a manner similar to our previous reports.[36−39]

The crystallinity and orientation of the as-deposited films were determined by X-ray diffraction (XRD) using a Bruker D8 Focus Diffractometer (equipped with a Lynx Eye Position Sensitive Detector) with Cu−Kα source (λ = 1.54439 Å). While performing the XRD scans, care was taken to avoid peak shifts in the XRD patterns due to sample misalignment. XRD rocking curves were performed using an in-plane grazing incidence configuration in order to maximize the signal from the in-plane direction of the films. The surface morphologies of the films were studied using an atomic force microscope (AFM) from Digital Instruments. The interfacial microstructure in the α-PLD-deposited CFO thin films was analyzed using high-resolution transmission electron microscopy (HRTEM) (FEI Tecnai F 20 S-Twin TEM). The sample for cross-sectional HRTEM analysis was prepared by milling out a 5 μm × 10 μm rectangular strip that was 100 nm in thickness from the film surface using a focused ion beam (FIB) (JEOL 4500 FIB/SEM) and Pt-welding it to a Cu TEM grid.

The magnetic properties of the CFO thin films were measured at room temperature using a commercial Physical property measurement system (PPMS) from Quantum Design equipped with a vibrating sample magnetometer (VSM) in magnetic fields up to 5 T applied parallel to the film plane. For magnetic measurements, all the thin films were cut to the same rectangular sizes of 2 mm × 3 mm and they were all aligned with their longer lengths parallel to the magnetic field inside the PPMS to avoid errors associated with different shapes of samples. The magnetization versus magnetic field (M−H) curves presented here were obtained after subtracting the diamagnetic contribution from the Si substrates.

3. RESULTS AND DISCUSSION

Henceforth in the text the nomenclatures "α-PLD" and "90°-PLD" will be used to distinguish between oblique- and normal-incidence pulsed laser deposition processes, respectively.

3.1. In Situ Optical Plume Diagnostics. In the PLD process, after the laser interacts with the target surface the evaporated target material forms a plasma of highly excited and ionized species which on subsequent expansion and collisional excitation extends in a visible plume of material traveling from the target to the substrate.[40] In situ plume imaging is a noninvasive probe that provides a two-dimensional snapshot of the plume propagation and dynamics that is critical for the optimization of the film growth parameters.[41] Figure 1 shows the time-integrated ICCD image of the total visible emission from the laser-induced plume during the optimized growth of α-PLD-deposited CFO thin films. The position of the target, the laser beam and the 120°-tilted substrate have been schematically drawn to-scale to show their real positions in space with respect to the plume. As depicted in the figure the most intense region (higher counts) of the visible plume close to the target surface gradually fades and completely disappears at least 2 cm before the substrate surface. The spatial expansion of the plume with respect to the angle of tilt of the substrates was critical for the optimized growth of uniform thin films with smooth surface morphologies. From preliminary experiments it was observed that using large oblique angles such as 175° (where the substrate was almost parallel to the plume) during the film growth, undesirable nonuniform films are produced that exhibit large density of pits and pores due to the excessive shadowing effects at such large incidence angles (see the Supporting Information, Figure S1).[42] Also, it was found that smaller target−substrate distances (<4 cm), higher laser fluences (>2 J/cm^2), or high background ambient gas pressures (>100 mTorr) during the film growth lead to the deposition of particulate-laden films with rough surface morphologies.

3.2. Crystallinity and Surface Morphology. Figures 2a−d show the XRD θ−2θ patterns for the α-PLD deposited CFO thin films with varying thicknesses of 400, 200, 100, and 50 nm, respectively. In all the patterns, the observed peaks were indexed to the face-centered cubic phase of CFO with a space group of $Fd\bar{3}m$ (227). The XRD pattern of the 400 nm thick film demonstrates a bulklike polycrystalline nature (Figure 2a).[7,8] On the other hand, the XRD patterns for the 200, 100, and 50 nm thick CFO films show preferred orientation in the CFO (111) crystallographic plane (Figures 2b−d). From Figure 2, it is clear that the CFO (111) crystal orientation is the preferred growth direction for CFO thin films below a critical thickness of 200 nm.[7,15,43] Panels a and b in Figure 3 show the XRD θ−2θ patterns of the 200 nm thick CFO thin films grown under the same conditions using α-PLD and 90°-PLD, respectively. While the α-PLD deposited CFO film shows preferred (111) orientation, the 90°-PLD film shows randomly oriented polycrystalline nature. The insets to panels a and b in Figure 3 show the XRD rocking curves performed about the CFO (222) crystallographic plane for the α-PLD and 90°-PLD grown films, respectively. The smaller full-width-at-half-maxima (fwhm) value of the rocking curve peak in the α-PLD deposited film (fwhm = 0.18°) as compared to that of the 90°-PLD film (fwhm = 0.41°) indicated the better in-plane orientation of the (111) plane (Figure 3) in the α-PLD grown film as compared to the 90°-PLD film. The results indicate that α-PLD grown films had enhanced texturing as compared to those grown using 90°-PLD.

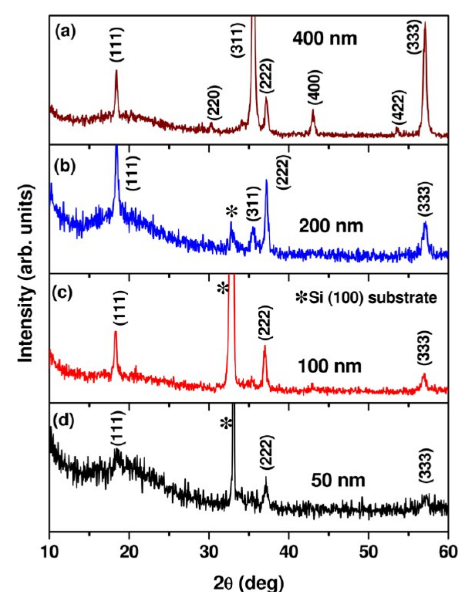

Figure 2. XRD θ−2θ patterns for CFO thin films deposited on Si substrates using oblique-angle PLD under the same conditions for varying thicknesses of (a) 400, (b) 200, (c) 100, and (d) 50 nm, respectively. The Si substrate peaks have been marked as *.

We calculated the lattice parameters (a) and lattice strains (ε) of the deposited films from their XRD θ−2θ scans and using the relation $\varepsilon = (a - a_o)/a_o$, where a is the average lattice parameter of the film and a_o is the bulk unstressed lattice parameter of CFO (a_o = 8.39 Å), as measured from the CFO powder.[7] For these calculations all the XRD patterns were

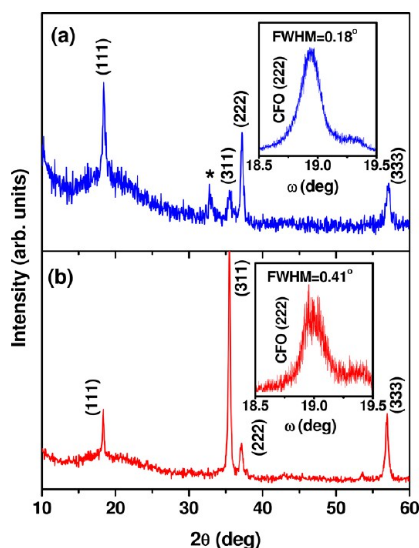

Figure 3. XRD $\theta-2\theta$ patterns for 200 nm thick CFO thin films deposited on Si substrates using (a) oblique and (b) normal-incidence PLD processes keeping all other parameters constant, respectively. The insets show the XRD rocking curves performed about the CFO (222) planes for the respective films.

matched with the Si substrate peak which was considered as the standard. Crystallite sizes (D_{Sch}) were calculated using the Scherrer formula assuming spherical crystallites as $D_{Sch} = 4/3L$ where L is given by eq 1[44,45]

$$L = \frac{\kappa\lambda}{B\cos\theta} \quad (1)$$

where L is the coherence length of reflected X-rays, κ is the particle shape factor (for spherical particles, $\kappa = 0.94$), λ is the wavelength of X-rays (for CuKα, $\lambda = 1.54439$ Å), B is the full width at half-maxima (fwhm) of $\theta-2\theta$ peak, and θ is the angle of diffraction.

The lattice strains (η) and crystallite sizes (D_{WH}) for each sample were also calculated independently using the Williamson–Hall method, which follows eq 2[46]

$$B\cos\theta/\lambda = \eta\sin\theta/\lambda + 1/D_{WH} \quad (2)$$

where B is the fwhm of $\theta-2\theta$ peak, θ is the diffraction angle, λ is the X-ray wavelength, η is the effective strain, and D_{WH} is the effective crystallite size.

The strain (η) was calculated from the slope and the crystallite size (D_{WH}) was calculated from the intercept of a plot of $B\cos\theta/\lambda$ against $\sin\theta/\lambda$ (as shown in the Supporting Information, Figure S2). The calculated a, ε, D_{Sch}, η, and D_{WH} values have been summarized in Table 1. From the a and ε values in Table 1, it is clear that α-PLD-deposited CFO films showed decreased a values as compared to a_o resulting in large compressive strains ($\varepsilon < 0$) in the films. On the other hand, the 90°-PLD deposited CFO films showed slightly increased a values as compared to a_o resulting in small tensile strains ($\varepsilon > 0$) in the films.[7] An analogous trend in effective strains (η) can also be seen in Table 1 as obtained from the Williamson–Hall calculations. Crystallite sizes calculated using both Scherrer formula ($D_{Sch} \approx 23-32$ nm) and Williamson–Hall technique ($D_{WH} \approx 28-35$ nm) (see Table 1) were consistent with each other. These crystallite sizes were smaller than the critical single domain size for CFO (~40 nm) suggesting that the films were possibly composed of single-crystal nanograins.[47] The similar results obtained from the different techniques corroborated the fact that the observed trends in strains and crystallite sizes were real. A slight decrease in strain values (both ε and η in Table 1) is observed in the 200 nm thick films which could be associated with strain relaxation due to grain boundary effects.[48] It is to be noted that since the CFO films were grown under the same conditions on similar Si substrates, the compressive and tensile strains in α-PLD- and 90°-PLD-deposited CFO films, respectively, were not a result of lattice mismatch within the substrate as in the case of epitaxial CFO thin films but because of intrinsic difference in the microstructure of the films as a result of oblique or normal plume incidence in PLD.[8,20] The difference in strains in α-PLD- and 90°-PLD-deposited CFO films could contribute to their different magnetic properties.

Figure 4a–c show AFM images of the surface morphologies of α-PLD-grown CFO films with varying thicknesses of 50, 100, and 200 nm, respectively. In contrast, Figure 4d shows an AFM image of the 200 nm thick 90°-PLD-grown CFO film. In all cases, the direction of deposition has been indicated by arrows. All the scans have been shown using the same area of 2 × 2 μm^2 and z-height of 100 nm for comparison. The grain sizes and root-mean-square surface roughness (R_{rms}) values for all the samples are summarized in Table 1. As have been observed from the figure and the values in Table 1, the α-PLD deposited films exhibited extremely smooth surfaces (Figure 4a–c) with R_{rms} values varying as low as 1–2 nm (Table 1). On the other hand, the 90°-PLD-grown CFO films were relatively rough with

Table 1. Film Thickness, Lattice Parameter, Lattice Strain, Crystallite Size, Effective Strain and Crystallite Size, Grain Size, and RMS Surface Roughness Values[a]

					Williamson–Hall			
type of PLD	film thickness (nm)	lattice parameter a (Å)	strain ε (%)	crystallite size D_{Sch} (nm)	η (%)	D_{WH} (nm)	grain size G (nm)	roughness R_{rms} (nm)
oblique	50	8.358 ± 0.028	−0.39 ± 0.03	23 ± 2	−0.48	21	80 ± 25	1.3 ± 0.2
	100	8.350 ± 0.027	−0.49 ± 0.02	32 ± 3	−0.57	31	96 ± 18	1.2 ± 0.3
	200	8.353 ± 0.029	−0.45 ± 0.03	28 ± 5	−0.42	25	98 ± 7	1.7 ± 0.1
normal	50	8.392 ± 0.017	0.021 ± 0.010	28 ± 5	0.18	36	55 ± 6	9.4 ± 0.4
	100	8.398 ± 0.013	0.087 ± 0.015	35 ± 7	0.34	38	82 ± 5	10.6 ± 0.3
	200	8.396 ± 0.007	0.065 ± 0.009	34 ± 5	0.25	38	96 ± 9	11.5 ± 0.2

[a]Lattice parameter a calculated from XRD $\theta-2\theta$ scans, lattice strain (ε) calculated using $\varepsilon = (a - a_o)/a_o$ (where $a_o = 8.391$ Å is the bulk lattice parameter of CFO), crystallite size (D_{Sch}) calculated using Scherrer formula, effective strain (η) and crystallite size (D_{WH}) calculated using the Williamson–Hall method, grain size (G) and root-mean-square surface roughness (R_{rms}) obtained from AFM analysis for each CFO thin film at different thicknesess of 50, 100, and 200 nm deposited using both oblique and normal incidence PLD processes.

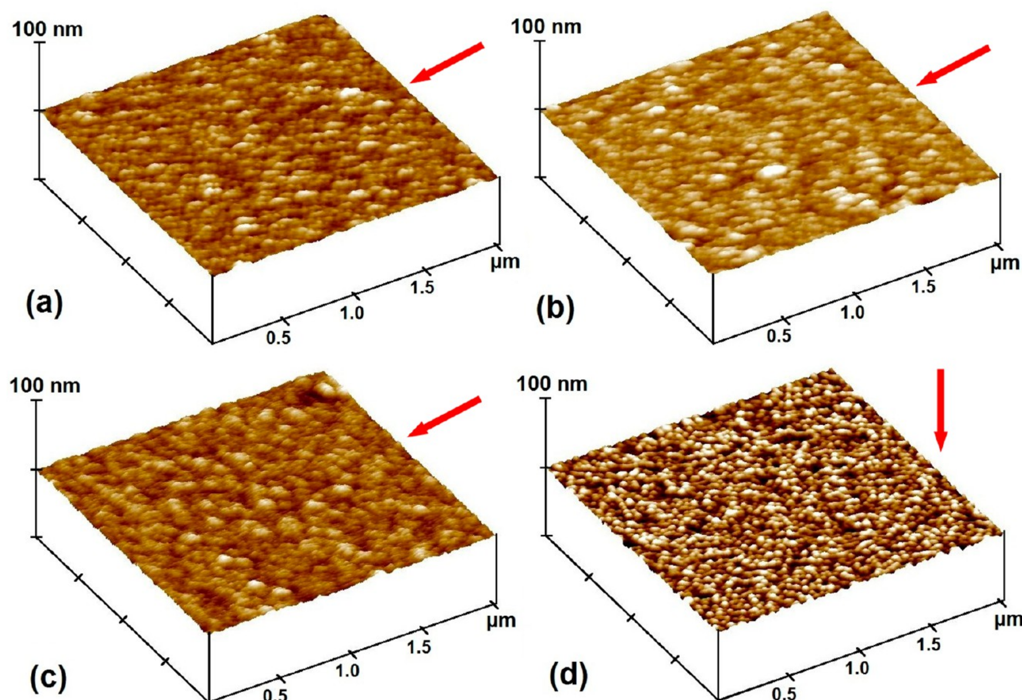

Figure 4. AFM images of the surfaces of CFO thin films deposited using oblique-angle PLD at varying thicknesses of (a) 50, (b) 100, and (c) 200 nm, and normal-incidence PLD at thickness of (d) 200 nm, respectively. The red arrow indicates the direction of deposition. All the scans have been shown using the same area of 2×2 μm^2 and z-height of 100 nm for comparison.

higher R_{rms} values in the range of 10−11 nm.[7,15] A systematic increase in R_{rms} with film thickness (Table 1) is observed in both α-PL and 90°-PLD-grown CFO films.[7,15] From Figure 4, it can also be seen that the surfaces of the α-PLD-deposited films exhibited nonuniform grain growth, which is not observed in the 90°-PLD-grown CFO film. The elongated and irregular grain shapes in the α-PLD deposited films (Figure 4a−c) were a result of bundling[49] and lateral fanning[50] of adjacent crystallites during the film growth in the α-PLD process.[32] Because the grain sizes obtained from AFM analysis are larger than the crystallite sizes obtained from XRD analysis (Table 1), it is possible that each grain is composed of multiple nanocrystallites. The distinctively different surface morphologies for α-PLD- and 90°-PLD-grown CFO films (Figure 4) suggested possible different growth mechanisms during the film deposition. Although the nonuniform grain sizes with low surface roughness in α-PLD-grown CFO films suggested an island-type growth mode, the small and uniform grain sizes suggested a layer-by-layer growth mode in the 90°-PLD grown CFO films similar to previous reports.[51]

3.3. Interfacial Microstructure and Growth Mechanism. To better understand the growth mechanisms in α-PLD, the interfacial microstructure of the α-PLD grown CFO films were studied using cross-sectional high resolution TEM (HRTEM). Figure 5a−c shows HRTEM images captured at different locations along the interface of a 200 nm thick α-PLD grown CFO film. An ultrathin (2−4 nm) layer of amorphous SiO_2 is present in all the images as a result of surface oxidation of single crystal Si (100) substrates. From the figure is can be seen that the CFO layer made a distinctly sharp and flat interface with the Si substrate. Distinct single-crystal columnar structures (shown by dotted lines in Figure 5) with continuous sharp lattice fringe spacings identified with the preferred (111) orientation of CFO are present in all the images. Within the

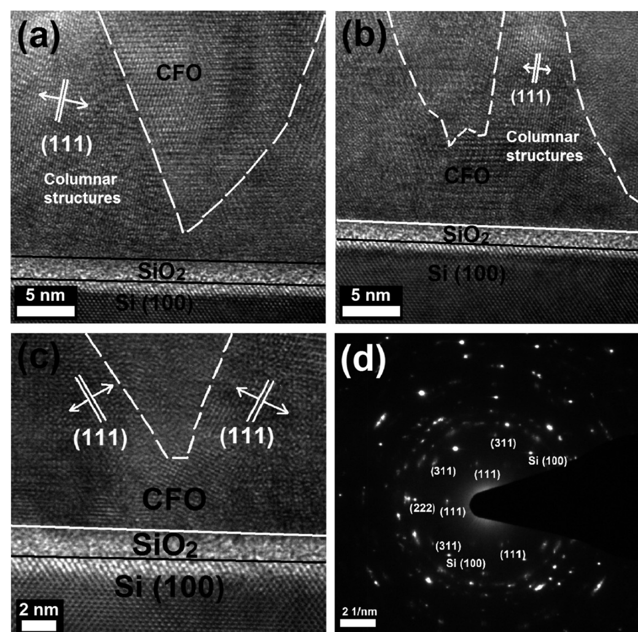

Figure 5. (a−c) Cross-sectional HRTEM images captured at different locations along the interface of the 200 nm thick CFO thin film deposited using oblique-angle PLD. (d) Typical SAED pattern obtained near the interface of the 200 nm thick CFO thin film deposited using oblique-angle PLD.

space between the columns, different order of lattice fringes corresponding with the (311) or (400) orientations of CFO are observed. Figure 5d shows the selected area electron diffraction (SAED) pattern obtained near the interface. Unlike the continuous ring patterns of a bulk polycrystalline sample, the SAED pattern in Figure 5d shows a dotted pattern indicating

dx.doi.org/10.1021/am401771z | ACS Appl. Mater. Interfaces 2013, 5, 7450−7457

preferential growth, corroborating the preferred crystal (111) orientation that was observed in the XRD analysis earlier. Such nanocolumnar interfaces as seen in Figure 5 were not observed in 90°-PLD-grown CFO films.

Figure 6 shows a schematic diagram of the various stages labeled as a−e of film growth as a function of the deposition time in both oblique- and normal-incidence deposition conditions. The initial stage is similar in both processes. As the flux of the laser-ablated species arrives at the substrates the smallest stable clusters nucleate on the substrate and grow into three-dimensional islands, with a preference to form more islands with the preferred (111) orientation (marked in red in Figure 6 a) which is the easy direction of growth for the CFO crystal. Deposition of CFO on amorphous SiO_2/Si substrates results in such island growth via the Volmer−Weber growth mechanism, typically observed when atoms being deposited are more strongly bonded to each other than to the dissimilar substrate material.[52] Unlike the growth of epitaxial CFO thin films on single-crystal substrates such as MgO (100) or $SrTiO_3$ (100) where the crystal lattice of the substrates assists the initial nucleation of the single-crystal islands,[8] here the presence of the amorphous SiO_2 layer on the Si substrates did not facilitate such growth of single-crystal islands. The followings stages are different in the two processes. As more obliquely incident vapor flux arrives in the α-PLD process, extreme atomic shadowing (Figure 6b) and limited adatom diffusion work together to produce small isolated columns, mostly in the CFO (111) preferred direction (marked in red in Figure 6c), growing in a vertical manner. On the other hand, in normal incidence, because there is no such shadowing effect, the islands tend to grow both laterally and vertically with no preference to columnar growth (Figure 6b, c). Also, the presence of the amorphous SiO_2 layer does not provide open access to the underlying Si (100) surface, and consequently does not allow the formation of more islands along the CFO (100) plane in normal-incidence deposition. Eventually, with more and more material arriving in oblique incidence, the dissimilar growth rates in the vertical and horizontal direction reaches an equilibrium and grain coalescence is reached as in the case of normal incidence (Figure 6c). Subsequent depositions lead to a layer-by-layer growth in both the processes via the Frank−Van der Merve growth mechanism.[52] At this stage, the depositing atoms see the already-deposited CFO layers and are more strongly bonded to the underlying CFO layers than to each other leading to growth in two dimensions and continuous film formation (Figure 6 d). The process continues with each layer being progressively less strongly bonded than the previous layer and ends when the bulk bonding strength is reached. Finally, this results in preferentially oriented films with nanocolumnar interfaces (marked in red in Figure 6e) in oblique incidence, and on the other side, it leads to randomly oriented polycrystalline films in normal incidence (Figure 6e).

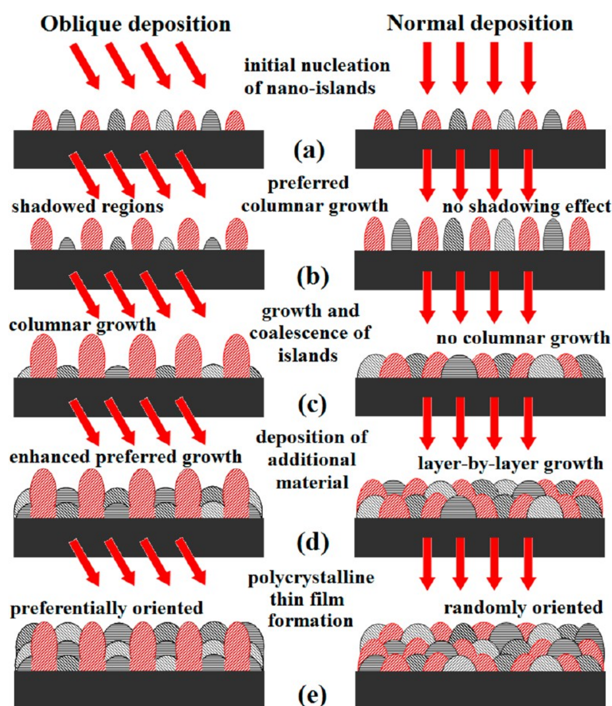

Figure 6. Schematic diagram showing the various stages of thin film growth mechanism as a function of the deposition time labeled as a−e in both oblique- and normal-incidence PLD processes.

3.4. Magnetic Properties.

Figure 7 shows the M−H hysteresis curves recorded at room temperature for the α-PLD grown CFO thin films with different thicknesses. As observed from the figure, the 100 and 200 nm thick α-PLD grown CFO films have comparable saturation magnetization (M_{sat}) and coercive fields (H_c) whereas the 50 nm thick film exhibited lower values of M_{sat} and H_c. The magnetic saturation of the 50 nm film were possibly diminished by the lower crystallinity in the film as indicated by the low-angle amorphous background in the XRD pattern (Figure 2) and the slightly lower compressive strain in the film (Table 1). Table 2 summarizes the M_{sat} and H_c values for all the samples along with their squareness factors (i.e., remanent magnetization (M_r) to M_{sat} ratio). Typically in hard magnets such as CFO the squareness and coercivity are considered as figures of merit for device applications.

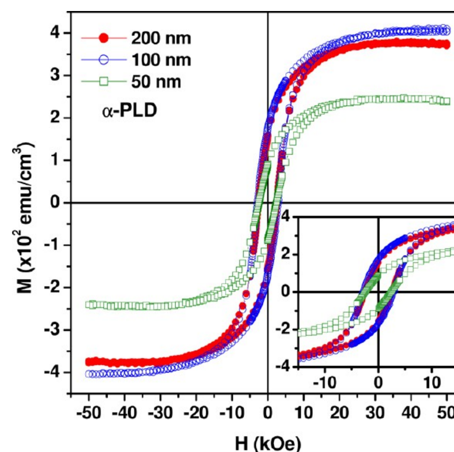

Figure 7. Magnetization vs magnetic field (M−H) hysteresis curves for CFO thin films grown using oblique-angle PLD under the same conditions with varying thicknesses of 50, 100, and 200 nm. The inset shows the enlarged portion of the M−H curves at low field ranges.

From the magnetic values in Table 2, the following observations are evident:

(I) M_{sat} values for α-PLD- and 90°-PLD-grown CFO films were comparable to each other and followed similar trends as function of the film thicknesses. The M_{sat} values observed in the 100 nm ($\approx$ 3.2 to 3.5 μ_B per Co^{2+} site) and 200 nm ($\approx$ 3.0 to

Table 2. Saturation Magnetization (M_{sat}), and Squareness (i.e., Remanent Magnetization (M_r) to M_{sat} ratio (M_r/M_{sat})), and Coercivity (H_c) Values for CFO Thin Films at Different Thicknesses of 50, 100, and 200 nm Deposited Using Both Oblique and Normal-Incidence PLD Processes

			magnetic properties			
type of PLD	angle of plume incidence (deg)	film thickness (nm)	M_{sat} (emu/cm^3)	M_{sat} (μ_B/Co^{2+})	M_r/M_{sat}	H_c(kOe)
oblique	120	50	242 ± 3	1.9	37	2.5
	120	100	402 ± 2	3.2	43	2.8
	120	200	376 ± 5	3.0	41	2.6
normal	90	50	351 ± 2	2.8	14	0.2
	90	100	440 ± 3	3.5	15	0.3
	90	200	417 ± 2	3.3	27	1.2

3.3 μ_B/Co^{2+}) thick CFO films in both cases were close to the theoretical saturation value of 3 μ_B/Co^{2+} for CFO.[1]

(II) Squareness factors for α-PLD-grown CFO films were almost 2−3 times higher that those grown using 90°-PLD process for all thicknesses as result of higher M_r, which is necessary for device applications. Although the squareness factors for 90°-PLD-grown CFO films matched with the previous report,[7] the enhanced squareness factors for α-PLD-grown CFO films matched well with those for epitaxial CFO thin films grown on single-crystal MgO (100) substrates using PLD.[8,20]

(III) H_c values for α-PLD-grown CFO films were almost 10 times higher than those grown using 90°-PLD process. To the best of our knowledge, the in-plane H_c values of 2.5−2.8 kOe observed for α-PLD-grown CFO films (Table 2) are one of the highest values ever reported for any in situ grown polycrystalline CFO films. Reported H_c values vary from 0.2 to 1.2 kOe for as-grown CFO films with one of the highest H_c values reported as 7.5 kOe for CFO films grown using rf sputtering process, but requiring ex situ post annealing at 900 °C in air for 2 h.[15−19,22,53]

To clearly demonstrate the enhanced magnetic properties of α-PLD-grown CFO thin films, we have shown the M−H curves for both α-PLD- and 90°-PLD-deposited CFO films at thicknesses of 100 and 200 nm in panels a and b in Figure 8, respectively. It is worth noting in this figure that there is a kink in the M−H loops near zero field for 90°-PLD-grown CFO films, whereas this feature is absent for α-PLD-grown CFO films. The noted kink, which has also been observed in 90°-PLD-grown CFO films on Si(100) and Al_2O_3(0001) substrates,[7] can be attributed to the presence of the tensile strain that tends to generate a perpendicular magnetic anisotropy because of a negative magnetostriction constant of the CFO film[20] and competing with the magnetocrystalline anisotropy and the magnetic shape anisotropy of the two-dimensional film. It can also be related to the lack of a well-defined crystalline structure (the possible presence of an amorphous magnetic layer) at the interface between the film and SiO_2 layer in 90°-PLD grown CFO films, as evidenced from TEM images. This effect is significant in thin films and becomes less significant in thick films, as the crystalline structure is more defined in thicker films. This explains why the kinklike feature is strongly suppressed in the 200 nm thick CFO film (Figure 8b) as compared to the 100 nm thick CFO film (Figure 8a). It is the presence of the kink that resulted in the overall reduction of H_c and M_r/M_s ratio for 90°-PLD-grown

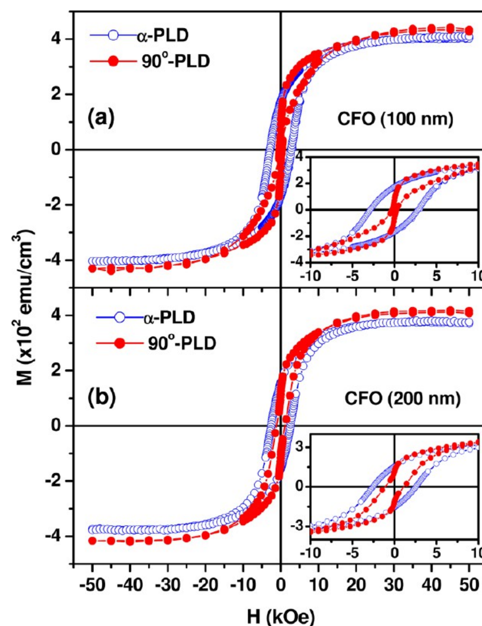

Figure 8. Magnetization vs magnetic field (M−H) hysteresis curves for CFO thin films deposited using both oblique- and normal-incidence PLD process labeled as α-PLD and 90°-PLD at thicknesses of 100 and 200 nm, respectively. The insets show the enlarged portion of the M−H curves at low field ranges.

CFO films. However, the case is different for α-PLD-grown CFO films, where the single-crystalline nanocolumns formed at the interfaces showing the (111) crystal orientation (Figure 5) resulted in enhanced preferred growth along the CFO (111) direction (i.e., along the hard axis of magnetization for single-crystal CFO), possibly resulting in the increased magnetocrystalline anisotropy and higher M_r values. Strain-induced higher coercivity where domain wall motion is restricted as a result of strain was reported in CFO thin films.[54] From XRD strain analysis (Table 1), it was observed that the α-PLD-grown CFO thin films exhibited higher compressive strains, as compared to the slightly tensile strains in the 90°-PLD-grown CFO films, which most probably resulted in the higher H_c values.

4. CONCLUSIONS

In conclusion, CFO thin films were deposited under the same conditions using oblique and normal-incidence PLD processes. XRD analyses revealed an enhanced preferred orientation along the CFO (111) plane in the oblique-incident films, while AFM images revealed extremely smooth film surfaces as compared to the normal-incident deposited films. HRTEM images of the obliquely incident CFO films showed nanocolumnar growth along the interfaces in the preferred CFO (111) direction. Magnetization measurements showed comparable saturation magnetizations in both oblique and normal-incident CFO films; however, a huge systematic enhancement in the coercive fields was obtained in the obliquely incident CFO films as compared to those deposited using normal-incidence PLD. Textured CFO thin films with nanocolumnar interfaces with tunable and enhanced coercivity can enable their potential application in magneto-optic devices.

■ ASSOCIATED CONTENT

Ⓢ Supporting Information

Schematic diagrams of substrate, target, and plume at large oblique-angle incidence deposition, AFM images showing pits and pores of films deposited at large incidence angles, schematic diagrams of extreme shadowing effect, Williamson–Hall plots, and table of strain and crystallite sizes for CFO films. This material is available free of charge via the Internet at http://pubs.acs.org/.

■ AUTHOR INFORMATION

Corresponding Author

*E-mail: dmukherj@usf.edu.

Notes

The authors declare no competing financial interest.

■ ACKNOWLEDGMENTS

This work was supported by the United States Army (Grant W81XWH1020101/3349).

■ REFERENCES

(1) Bozorth, R. M. *Ferromagnetism*, 6th ed.; D. Van Nostrand Company: New York, 1961.
(2) Goldman, A. *Modern Ferrite Technology*, 2nd ed.; Springer: New York, 2006.
(3) Dorsey, P. C.; Lubitz, P.; Chrisey, D. B.; Horwitz, J. S. *J. Appl. Phys.* **1996**, *79*, 6338–6340.
(4) Chapline, M.; Wang, S. *Phys. Rev. B* **2006**, *74*, 014418.
(5) Caltun, O. F.; Rao, G. S. N.; Rao, K. H.; Rao, B. P.; Kim, C.; Kim, C.-O.; Dumitru, I.; Lupu, N.; Chiriac, H. *Sensor Lett.* **2007**, *5*, 45–47.
(6) Rendale, M. K.; Kulkarni, S. D.; Puri, V. *Microelectron. Int.* **2009**, *26*, 43–46.
(7) Mukherjee, D.; Dhakal, T.; Phan, M. H.; Srikanth, H.; Mukherjee, P.; Witanachchi, S. *Physica. B. Condens. Matter.* **2011**, *406*, 2663–2668.
(8) Dhakal, T.; Mukherjee, D.; Hyde, R.; Mukherjee, P.; Phan, M. H.; Srikanth, H.; Witanachchi, S. *J. Appl. Phys.* **2010**, *107*, 053914.
(9) Huang, W.; Zhu, J.; Zeng, H. Z.; Wei, X. H.; Zhang, Y.; Li, Y. R. *Appl. Phys. Lett.* **2006**, *89*, 262506.
(10) Terzzoli, M. C.; Duhalde, S.; Jacobo, S.; Steren, L.; Moina, C. *J. Alloys Compd.* **2004**, *369*, 209–212.
(11) Hiratsuka, N.; Nozawa, M.; Kakizaki, K. *J. Magn. Soc. Jpn.* **1996**, *20*, 53–56.
(12) Okuno, S. N.; Hashimoto, S.; Inomata, K. *J. Appl. Phys.* **1992**, *71*, 5926–5929.
(13) Pramanik, N. C.; Fujii, T.; Nakanishi, M.; Takada, J. *Mater. Lett.* **2005**, *59*, 88–93.
(14) Lee, J. G.; Park, J. Y.; Oh, Y. J.; Kim, C. S. *J. Appl. Phys.* **1998**, *84*, 2801–2804.
(15) Raghunathan, A.; Nlebedim, I. C.; Jiles, D. C.; Snyder, J. E. *J. Appl. Phys.* **2010**, *107*, 09A516.
(16) Araújo, C.; Almeida, B. G.; Aguiar, M.; Mendes, J. A. *Vacuum* **2008**, *82*, 1437–1440.
(17) Gao, X. S.; Bao, D. H.; Birajdar, B.; Habisreuther, T.; Mattheis, R.; Schubert, M. A.; Alexe, M.; Hesse, D. *J. Phys. D: Appl. Phys.* **2009**, *42*, 175006.
(18) Ning, M.; Li, J.; Ong, C. K.; Wang, S. J. *J. Appl. Phys.* **2008**, *103*, 013911.
(19) Thang, P. D.; Rijnders, G.; Blank, D. H. A. *J. Magn. Magn. Mater.* **2007**, *310*, 2621–2623.
(20) Mukherjee, D.; Dhakal, T.; Hyde, R.; Mukherjee, P.; Srikanth, H.; Witanachchi, S. *J. Phys. D: Appl. Phys.* **2010**, *43*, 485001.
(21) Wang, X. W.; Zhang, Y. Q.; Meng, H.; Wang, Z. J.; Zhang, Z. D. *J. Alloys Compd.* **2011**, *509*, 7803–7807.
(22) Wang, Y. C.; Ding, J.; Yi, J. B.; Liu, B. H.; Yu, T.; Shen, Z. X. *Appl. Phys. Lett.* **2004**, *84*, 2596–2598.
(23) Robbie, K.; Beydaghyan, G.; Brown, T.; Dean, C.; Adams, J.; Buzea, C. *Rev. Sci. Instrum.* **2004**, *75*, 1089–1097.
(24) Robbie, K.; Brett, M. J. *J. Vac. Sci. Technol. A.* **1997**, *15*, 1460–1465.
(25) Karabacak, T.; Mallikarjunan, A.; Singh, J. P.; Ye, D.; Wang, G. C.; Lu, T. M. *Appl. Phys. Lett.* **2003**, *83*, 3096–3098.
(26) Shim, Y.; Amar, J. G. *Phys. Rev. Lett.* **2007**, *98*, 046103.
(27) Ye, D. X.; Zhao, Y. P.; Yang, G. R.; Zhao, Y. G.; Wang, G. C.; Lu, T. M. *Nanotechnology* **2002**, *13*, 615–618.
(28) Ma, Y.; Liu, F.; Zhu, M.; Liu, J.; Wang, H.; Yang, Y.; Li, Y. *Nanotechnology* **2009**, *20*, 275201.
(29) Drotar, J.; Zhao, Y.-P.; Lu, T.-M.; Wang, G. C. *Phys. Rev. B* **2000**, *62*, 2118–2125.
(30) Shim, Y.; Borovikov, V.; Amar, J. G. *Phys. Rev. B* **2008**, *77*, 235423.
(31) Mayr, S. G.; Samwer, K. *J. Appl. Phys.* **2002**, *91*, 2779–2784.
(32) Wang, H.; Zhao, Y. P. *J. Vac. Sci. Technol. B. Microelectron. Nanometer. Struct. Process. Meas. Phenom.* **2006**, *24*, 1230–1233.
(33) Chen, A.; Bi, Z.; Tsai, C. F.; Chen, L.; Su, Q.; Zhang, X.; Wang, H. *Cryst. Growth. Des.* **2011**, *11*, 5405–5409.
(34) Witanachchi, S.; Mukherjee, P. *J. Appl. Phys.* **1995**, *78*, 4099–4103.
(35) Schey, B.; Biegel, W.; Kuhn, M.; Stritzker, B. *Appl. Phys. A-Mater.* **1999**, *69*, S419–S422.
(36) Mukherjee, P.; Chen, S.; Witanachchi, S. *Appl. Phys. Lett.* **1999**, *74*, 1546–1548.
(37) Hyde, R. H. Growth and Characterization of Thermoelectric $Ba_8Ga_{16}Ge_{30}$ Type-I Clathrate Thin-Films Deposited by Pulsed Dual-Laser Ablation. *Ph.D. Dissertation*, University of South Florida, Tampa, FL, 2011.
(38) Mukherjee, D.; Hyde, R.; Mukherjee, P.; Srikanth, H.; Witanachchi, S. *J. Appl. Phys.* **2012**, *111*, 089905.
(39) Mukherjee, D.; Hyde, R.; Hordagoda, M.; Bingham, N.; Srikanth, H.; Witanachchi, S.; Mukherjee, P. *J. Appl. Phys.* **2012**, *112*, 064101.
(40) Geohegan, D. B. In *Pulsed Laser Deposition of Thin Films*; Chrisey, D. B., Hubler, G. K., Eds.; Wiley: New York, 1994; pp 115–165.
(41) Hirata, T.; Miyazaki, Z. *Anal. Chem.* **2007**, *79*, 147–52.
(42) Kranenburg, H.; van Lodder, C. *Mater. Sci. Eng. R. Rep.* **1994**, *11*, 295–354.
(43) Yin, J. H.; Ding, J.; Liu, B. H.; Miao, X. S.; Chen, J. S. *J. Magn. Magn. Mater.* **2007**, *310*, 2537–2539.
(44) Cullity, B. D. *Elements of X-Ray Diffraction*, 2nd ed.; Addison-Wesley: New York, 1978.
(45) Klug, H. P.; Alexander, L. E. *X-Ray Diffraction Procedures: For Polycrystalline and Amorphous Materials*, 2nd ed.; Wiley-Interscience: New York, 1974.
(46) Williamson, G. K.; Hall, W. H. *Acta. Metall.* **1953**, *1*, 22–31.
(47) Chinnasamy, C. N.; Jeyadevan, B.; Shinoda, K.; Tohji, K.; Djayaprawira, D. J.; Takahashi, M.; Joseyphus, R. J.; Narayanasamy, A. *Appl. Phys. Lett.* **2003**, *83*, 2862–2864.
(48) Janssen, G. C. A. M. *Thin Solid Films* **2007**, *515*, 6654–6664.
(49) Zhao, Y.-P.; Ye, D.-X.; Wang, G.-C.; Lu, T.-M. *Nano Lett.* **2002**, *2*, 351–354.
(50) Vick, D.; Smy, T.; Brett, M. J. *J. Mater. Res.* **2011**, *17*, 2904–2911.
(51) Huang, W.; Zhou, L. X.; Zeng, H. Z.; Wei, X. H.; Zhu, J.; Zhang, Y.; Li, Y. R. *J. Cryst. Growth* **2007**, *300*, 426–430.
(52) Ohring, M. *Materials Science of Thin Films*, 2nd ed.; Academic Press: New York, 2001.
(53) Ding, J.; Chen, Y. J.; Shi, Y.; Wang, S. *Appl. Phys. Lett.* **2000**, *77*, 3621.
(54) Lisfi, A.; Williams, C. M. *J. Appl. Phys.* **2003**, *93*, 8143–8145.